Insights into crystallographic and topographic characteristics of local corrosion attack on zinc

Document Version
Final published version

Citation for published version (APA):
Withers, P., Zhong, X., Guo, Y., Zhou, X., & Cole, I. (in press). Insights into crystallographic and topographic characteristics of local corrosion attack on zinc. *Corrosion Engineering Science and Technology*, *58*(7), 667-675.

Published in:
Corrosion Engineering Science and Technology

OPEN ACCESS

Insights into crystallographic and topographic characteristics of local corrosion attack on zinc

Xiangli Zhong, Philip J. Withers, Yi Guo, Xiaorong Zhou & Ivan S. Cole

Published online: 05 Sep 2023.

Submit your article to this journal ↗

Article views: 33

View related articles ↗

View Crossmark data ↗

I·M3
Institute of Materials,
Minerals & Mining

Taylor & Francis
Taylor & Francis Group

Insights into crystallographic and topographic characteristics of local corrosion attack on zinc

Xiangli Zhong [a], Philip J. Withers[a,b], Yi Guo[b*], Xiaorong Zhou[a] and Ivan S. Cole[c]

aDepartment of Materials, University of Manchester, Manchester, UK; bDepartment of Materials, Henry Royce Institute, University of Manchester, Manchester, UK; cSchool of Engineering, RMIT University, Melbourne, Australia

ABSTRACT

Through large area crystallographic analysis across the whole cross-section of a 0.5 mm zinc wire by backscattered electron diffraction (EBSD) excavated by plasma focused ion beam (pFIB) and topographic analysis by scanning electron microscopy (SEM), the crystallographic and topographic characteristics of corrosion on zinc are identified and correlated. Striated domains dominating the surface are the result of preferential dissolution of non-basal planes leaving (0001) plates intersecting the surface. Remnant fragments of zinc lie close to the original surface which is due to the combined effects of the initial protective film on the surface and the crystallographic corrosion. Three corrosion layers were found, namely from the outside inwards, a highly porous outer layer, a densified intermediate layer and an attacked layer.

Introduction

Historically, zinc has been considered to corrode through a general corrosion process, rather than a localised one. Nevertheless it is well established that oxide dissolution [1,2] is a critical element in the propagationof corrosion and that this can occur locally and that corrosion can initiate from local microstructural features (e.g. grain boundaries) on surface [3,4]. Furthermore, detailed studies based on single crystal zinc by Abayarathna et al. [5] have established that attack is very dependent of crystal orientation. For example in near neutral solutions, striated features were observed on corroded {1010} surfaces, while hexagonal pits were observed on the basal planes. Similar features have been observed on grains of the same orientation in polycrystalline surfaces. Other reaserch groups have also studied the effect of grain orientation on corrosion attack on single and polycrystalline zinc [5–8]. They found that the protective oxide formation was more complete on grains having low index grain orientations compared to high indexed ones. Shkirskiy [9] used nanoscale scanning electrochemical cell microscopy to map anodic and cathodic regions on polycrystalline zinc in acid environments. They found that electrochemical activities, both anodic and cathodic, were reduced on low index grains and that there was a strong correlation with Kohn–sham Density Functional Theory (DFT) simulations of hydrogen absorption and zinc dissolution. Differences in experimental conditions and in corrosion measurements make comparisons between these studies difficult, however they all highlight the importance of grain orientation on the initial corrosion hehaviour.

While the above studies were carried out on fresh surfaces, in the last two decades research has indicated that corrosion of zinc, particularly under oxides, can be localised [1,10,2]. Scanning vibration electrode technique (SVET)

studies by Mena et al. [11] provided direct electrochemical evidence of pitting in zinc in laboratory tests. They used SVET to study the distribution of anodes and cathodes on zinc in 1:1000 diluted ocean water. After 2 h they observed localised anodic and cathodic zones. Over the period of the test (5 h) the locations of the anodic zones shifted. They attributed this to the development of oxides blocking the initial pit development and allowing the anodic (pitting) zones to move to new locations. Cole et al. [12] conducted an extensive study of corrosion morphology of zinc under conditions characteristic of locations in Southeast Asia and Australia with severe marine/marine, industrial/industrial, marine/industrial, and urban/ highland environments over a period of one year. Localised corrosion was observed in all cases. Cole et al. [13] carried out one of the first studies of oxide development and corrosion on zinc using focused ion beam - scanning electron microscopy (FIB-SEM). They exposed zinc to fine seawater droplets under controlled humidity for intervals ranging from 15 min to 6 h and observed the development of oxides and crystallographic corrosion. A three-layer structure of corrosion products built up over 6 h, comprising a zone below the original metal surface where oxide has filled in the volumes of corroded zinc (these corroded regions appeared to be along microstructural features), a zone above the original metal surface where the oxide is relatively compact, and a third zone above the first two where a highly porous crystalline corrosion product was observed. The first layer predominately comprised Zn and oxygen with some areas rich in zinc, oxygen and chlorine, the second layer contained zinc, oxygen and carbon layer containing zinc, oxygen, carbon and chlorine. After the build-up of an initial oxide the underlying metal was subject to localised attack that appeared to be along crystallographic features. Wang et al. [14] studied corrosion of a zinc wire immersed in 0.1m NaCl using

3D computed tomography (CT) and found the same layered structures.

In summary, recent research has demonstrated that localised corrosion may be important to zinc corrosion, particularly after an oxide layer has formed. However, it is not clear if this is to be regarded as 'true pitting' as the aspect ratios of the local attack were much lower than the pits observed in stainless steel or aluminium. In field observations, pitting appears to be associated with the local breakdown of oxide layers and thus the nature of oxide dissolution is critical to its formation. Pitting-like phenomena have also been observed in the early stages of corrosion in laboratory experiments which have also suggested crystallographic orientation may be important.

Here the aim has been to induce relatively rapid dissolution in zinc specimens and then to study the oxide formation and to investigate metal attack under the oxide to determine if local attack occurs and if it does to determine how it correlates with the crystallographic orientation [2,15].

To assist this study, a large area EBSD analysis method is proposed. The conventional method for EBSD samples involves mechanical polishing or electrochemical polishing [16] which may unintentionally modify the sample structure and compromise the EBSD results [17,18]. Here we utilise the dual-beam plasma focused ion beam (pFIB-SEM) for large cross-sectional milling of the whole wire surface followed by indirect EBSD analysis [19]. The EBSD results enable the correlation of the corrosion propagation paths with crystallographic orientation.

The paper addresses two specific questions,

1) What is the nature of the corrosion product layers and how do they vary in density/porosity and in composition?
2) What is the nature of attack on zinc under an oxide? – Previous work has identified localised attack [5,12,5].

Material and experimental procedures

Material and corrosion conditions

A 0.5 mm diameter zinc wire (99.9%, Goodfellow Metals) was placed in natural seawater under potentiostatic polarisation at a potential 260 mV positive to the open circuit potential (OCP, −1.26V versus saturated calomel electron (SCE)) for 24 h. The current quickly rose to a value of 7.9×10^{-5} amps/cm^2 and maintained that value throughout the 24 h period. This potential was chosen to generate a significant oxide film while not being too extreme in terms of possible potentials in the anodic zone of the corroding surface.

Electron microscopy

A variable pressure scanning electron microscope (VP SEM) (Hitachi S3000N) equipped with energy dispersive X-ray Spectrometer (EDS) from EDAX (Genesis 4.51) and a field emission SEM (FE-SEM) (Magellan ThermoFisher) were used for surface morphology and composition studies on a metallurgically prepared sample section. The corroded wire was embedded in a resin and metallurgically polished to 0.1μm diamond paste. The porosity of the corroded layers was inferred from the SEM images using the Fiji software [20] by dividing the cross-sectional pore area by the total material area. The density of the corrosion product was calculated by the product of the porosity and the zinc oxide density of 5.6 g/cm^3 [21]. To image the surface morphology of the corroded wire, the corrosion product was removed using a surgical knife blade and an in-house developed tool with a fine soft tip made from a polyethylene film.

A dual-beam microscope comprising an inductively coupled plasma Xe+ focused ion beam and field emission electron source (ThermoFisher Helios plasma FIB dual-beam system, hereafter referred to as a pFIB) was used for sectioning and imaging of serial sections of the sample [22]. Electron backscatter diffraction (EBSD) and secondary electron imaging were performed using Oxford instrument software Aztec 3.3 with a Nordlys fast EBSD detector and ThermoFisher pFIB operational software xT 9.4 with an Everhart–Thornley detector (ETD).

The ion beam milling for EBSD is preferred here because traditional metallogical polishing has a high probability of induced deformation on the surface leading to low hit rate in EBSD analysis [16]. However, conventional Ga$^+$ FIB is not commonly used for EBSD due to the limited milling dimensions, which are typically less than50μm. The recently developed dual-beam plasma Xe$^+$ FIB enables large area milling [22]. However ion beam damage of the target material has been a concern [23–25] due to ion beam – target interaction trajectories which could induce vacancies and interstitials in the target material thereby changing the atomic arrangment in the target material. In this study, the fast (7min) pFIB milling of Zn with minumiun surface damage is evidenced by the pFIB enabled EBSD analysis across the whole wire cross-section of 500 μm diameter. Comparing conventional Ga$^+$ FIB giving a sputtering yield of 57.1 atoms/ion on Zn with the highest avialable milling current of typically 65nA and the Xe+ plasma FIB giving a sputtering yield on Zn of 42.0 atoms/ion at the highest available milling current of 1300nA in this pFIB, the Xe$^+$ pFIB canprovide 25 times faster milling rate on Zn. However the highest milling rate on such a large area may result in surface roughness and damage reducing the EBSD indexing rate. Therefore, maintaininga high milling current without significantly reducing the EBSD indexing rate is cruicial in the optimisation of the milling process. At the same time, , EBSD was performed using a higher electron beam voltage to obtain a larger backscattered electron signal volume. A large collection volume withrespective to the ion beam damage surface layer may minimse the ngeative impact of the ion beam damaged layer. Monte Carlo simulation indicates the damage depth induced by 30kV ion beam interaction with the Zn wire (SRIM) [26] is within 10nm, the depth of backscattered electrons by 30kV electron beam interaction with the Zn wire (CASINO) [27] is more than 20nm. This indicates that the EBSD signals were mainly from beneath the top surface damage layer induced by ion beam milling. We acheived high quality EBSD maps with a pattern indexingrate of 95.8% using a milling current of 470nA which is ten times higherthan that which can be achieved using Ga+ FIB. A relatively rough surface with curtaining artefects along the milling direction was observed. This was caused by the large ion beam probe size having a gausian shape [28]. However, a
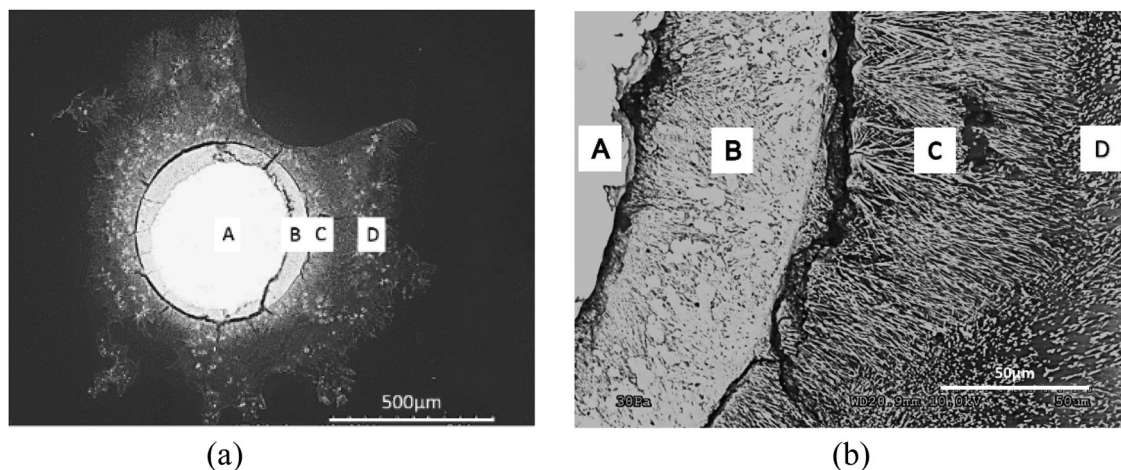
Figure 1. SEM image of the Zn wire after exposure in natural seawater under potentiostatic polarisation at 260 mV positive to the OCP (−1.26 V (SCE)) for 24 h. (a) the remaining uncorroded Zinc wire (A), the attacked layer (B), a dense layer (C) and a porous layer (D). (b) a higher magnification region of (a).

good EBSD indexing rate indicates that the effect of the surface is negligible. This study shows, for the first time, that EBSD analysis can be carried out on areas greater than n 500μm in diameter by fast pFIB milling provided the milling and EBSD conditions are optimised. The EBSD was performed at 30kV 11nA using a 0.44 μm step size after cross-sectioning using the optimised Xe^+ ion beam procedure. For good statistical calculation of the crystal planes at the corrosion front, the EBSD analysis was performed on 148 diametral serial section slices taken over a 0.25 mm length of the wire.

Results

Nature of the oxide layer

After exposure in natural seawater under potentiostatic polarisation at 260 mV positive to the OCP (−1.26V (SCE)) for 24 h, it can be seen from the SEM image in Figure 1 that there has been very extensive corrosion of the 0.5mm diameter wire. The extent of corrosion varies greatly, extending to 1-2mm laterally over the cross-section with the corrosion product extending between 0.1 and 0.4 mm from the original wire diameter. In common with previous observations, the SEM imaging suggests that the oxide contains 3 distinct layers. An outer layer (D) of loose flaky and porous oxide, an intermediate layer of relatively dense oxide (C) and within the boundary of the original wire a layer of dense oxide containing significant voids (B). Throughout the paper we will refer to these from the outside in as: the porous layer, the dense layer, and the attacked layer. In Figure 1, the porous layer (D) is shadowy and variable in intensity, the dense oxide (C) is somewhat brighter and the attacked layer (B) brightest of all. This may reflect changes in density as discussed later. The extents and porosities as determined by analysis of SEM image (Figure 1) of the various layers are summarised in Table 1.

Table 1. Level of porosity and the inferred net density.

	Avg. Dia. (μm)	Porosity (%)	Density (g/cm³)
Zn Wire	449	0	7.14
Attacked Layer	533	9.6	5.07
Dense layer	663	5.2	5.31
Loose layer	1178	18.7	4.56

Closer analysis of the interfacial region between the porous and attacked layer is shown in Figure 2 and Figure 3. A thin layer rich in C and O is evident on the outer surface of the zinc wire (Figure 2). It is evident in Figure 3 that there are voids in the attacked layer and that it contains regions of zinc that are decohered from the wire. Oxides in both the attacked and dense layers are crystalline. Both oxide layers are rich in zinc, oxide, and carbon, but the attacked layer has a higher Zn content whereas the dense layer has higher C and O contents (Figure 3). A small amount of Cl was detected in both layers, but the attacked layer has the higher Cl concentration. From Figures 2 and Figure 3 it is evident that larger voids are present in the attacked layer compared to the dense layer. Further, Figure 2 shows remnant metallic Zn in the regions immediately beneath the perimeter of the original zinc wire (as indicated by the red arrows in Figure 2).

Nature of Zinc attack

The interface between the attacked layer and the corroding metal surface is shown in Figure 4 and is characterised by a number of features including:

a) Large and relatively wide 'pits', ranging from 5 to 30 μm with aspect ratios up to 1.
b) Very narrow and deep 'pits' (which appear as striations in plane view, as shown later) from 5 to 20 μm in-depth which are very close to each other. Further, these narrow 'pits' may occur at the bottom of the wide 'pits'.

The morphology of these narrow and deep corrosion features, i.e. narrow 'pits', observed in Figure 4 are more easily discerned from the surface of the zinc once cleaned of corrosion products as shown in Figure 5. The striated domains (magnified inset) exemplifies the crystallographic nature of corrosion attack that reflects the underlying grain structure.

Crystallographic nature of attack

An extensive study of the crystallographic nature of the attack on zinc has been undertaken by characterising the cross-section of the corrosion front by combining pFIB serial
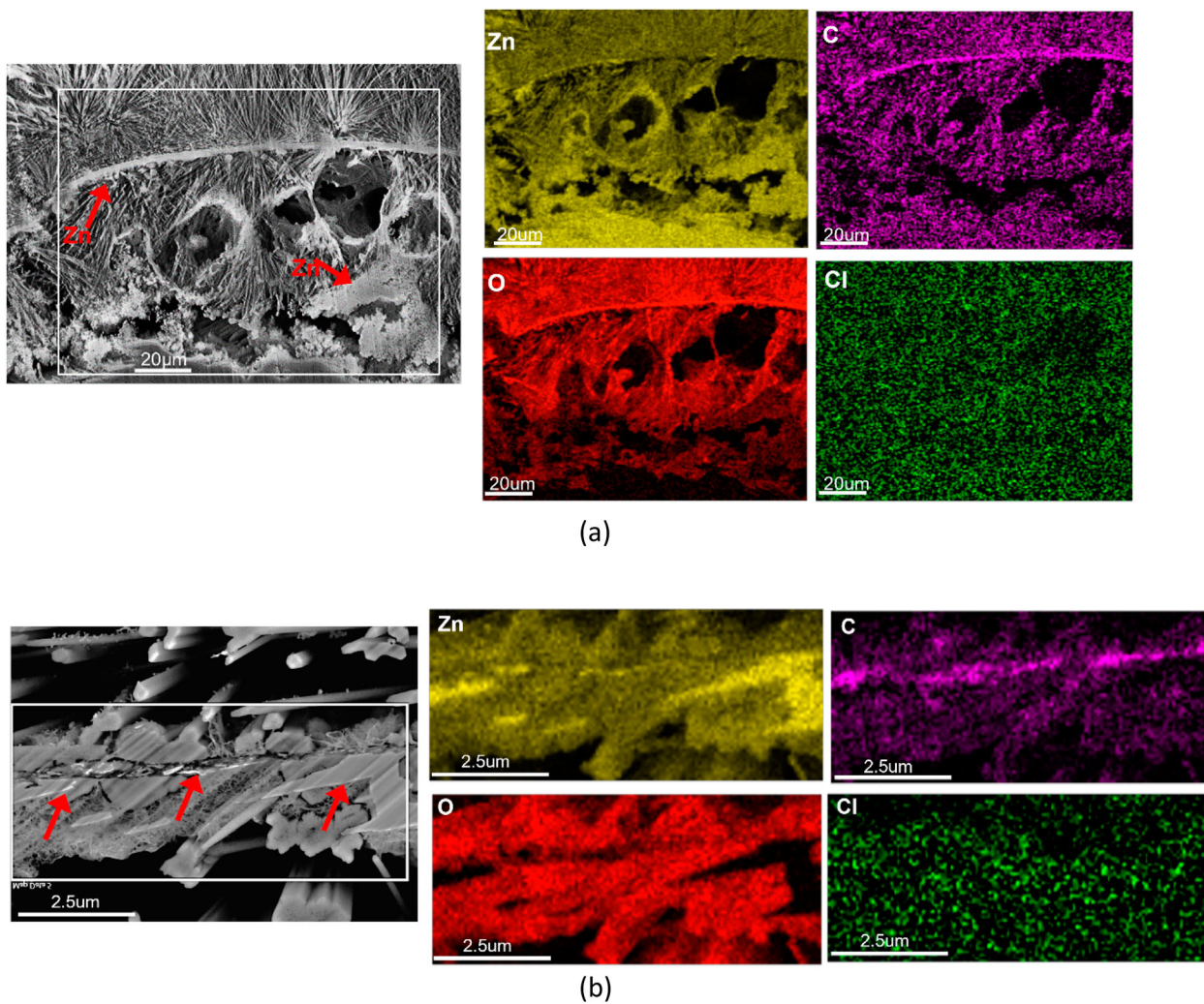
(a)

(b)

Figure 2. SEM and EDX of the two inner corrosion product layers: (a) the attacked layer contains large voids and has some remnant zinc (red arrows) embedded in the corrosion products; (b) higher magnification of the boundary between the dense and attacked layers showing crystalline oxide and remnant Zn (red arrows).
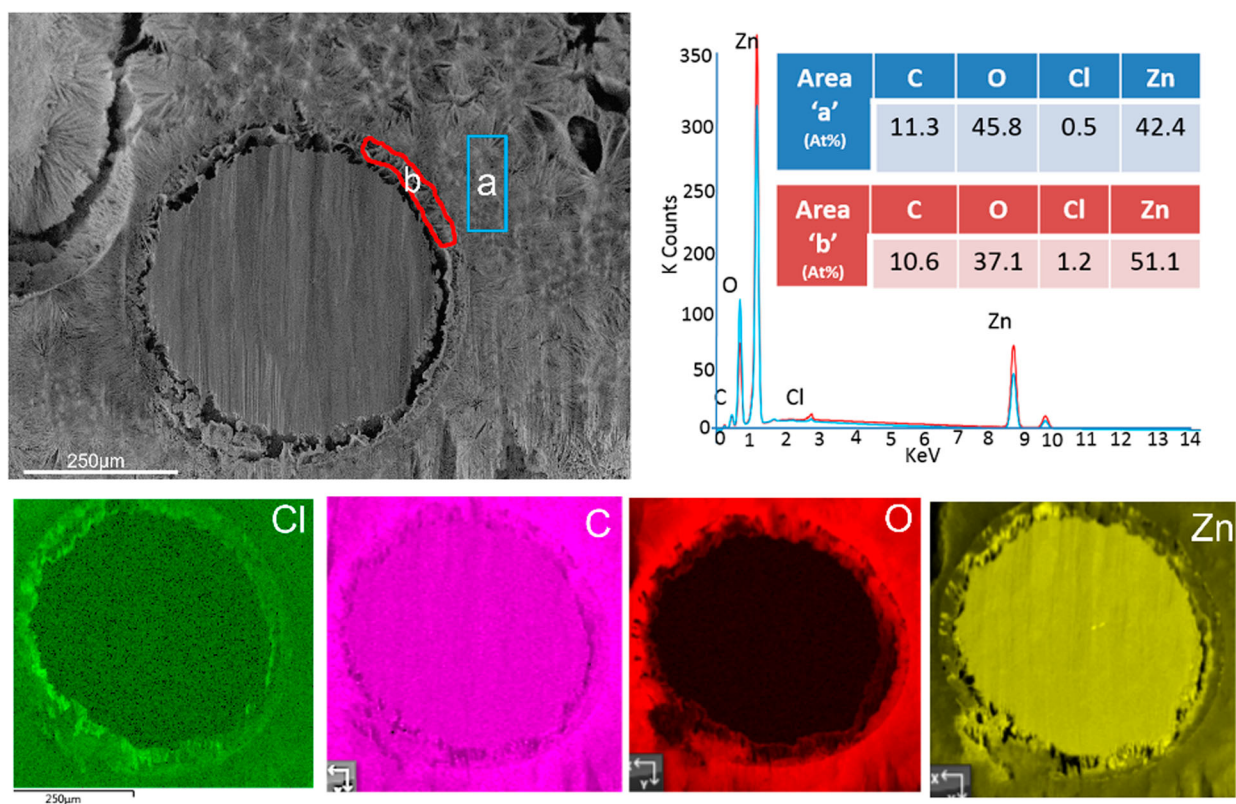

Area 'a' (At%)	C	O	Cl	Zn
	11.3	45.8	0.5	42.4

Area 'b' (At%)	C	O	Cl	Zn
	10.6	37.1	1.2	51.1

Figure 3. SEM image (top left) of a wire cross-section used for EDS mapping (below). The EDS sum spectra of area 'a' and 'b' are shown top right. The EDS maps show higher Cl but lower C and O concentration for the attacked layer 'b' compared to the dense layer 'a'.
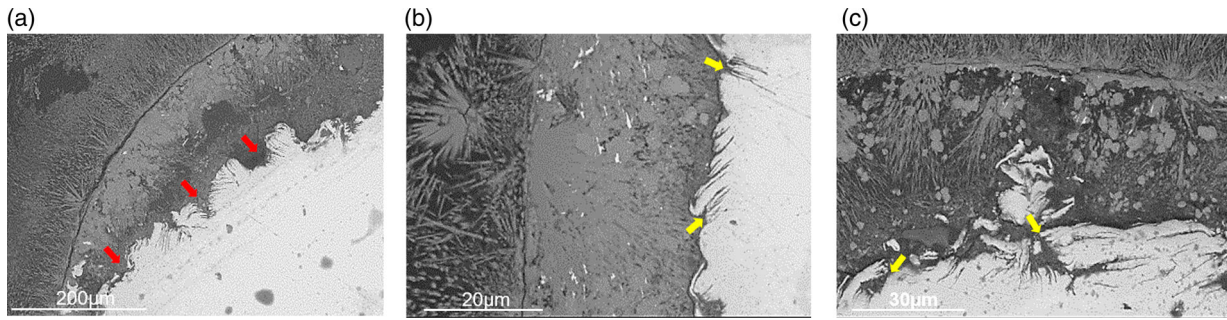
Figure 4. SEM micrographs of the metallic zinc-corrosion product interface: (a) relatively wide 'pits' or local areas of attack (red arrows), and (b)–(c) very narrow corrosion penetration extending 5–20 μm in depth (yellow arrows) represented by the striations in Figure 5.
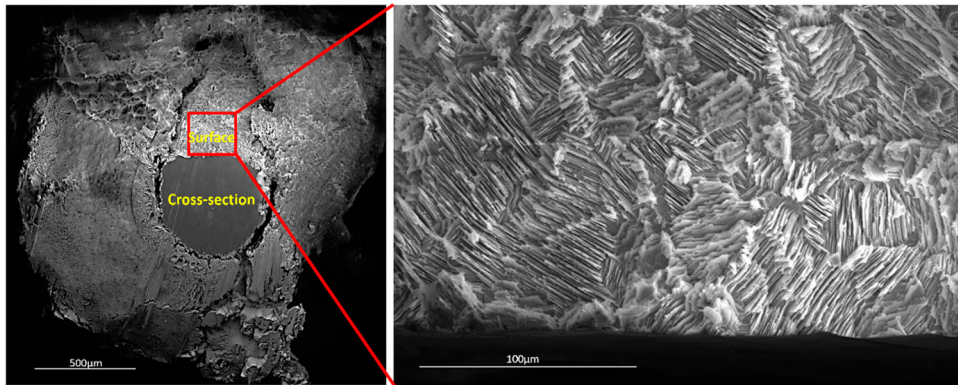

Figure 5. Topography of the attacked Zn wire surface after removal of corrosion products (surface is 38° to SEM electron column). The striated domain directions are determined by the orientation of the underlying grains.
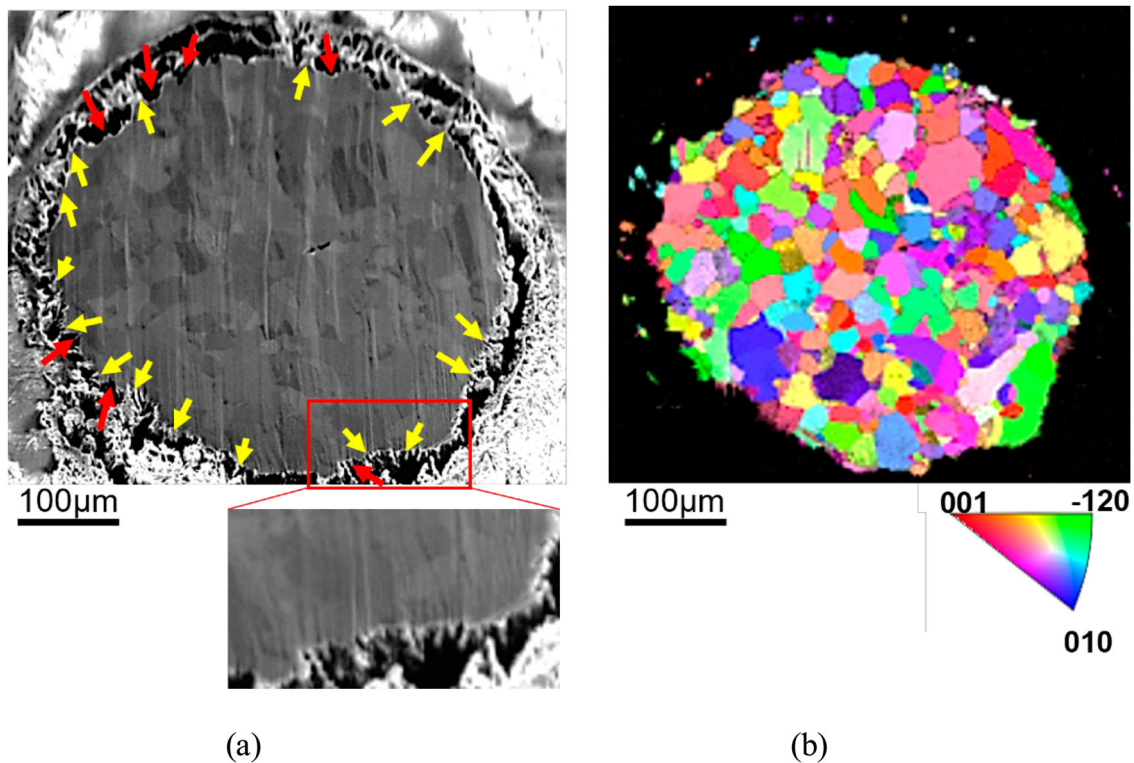

(a) (b)

Figure 6. (a) SE image and (b) EBSD inverse pole figure map of a cross-section of the corroded wire showing how the striations relate to the underlying crystallographic orientations. Some grains show more pronounced striations (yellow arrows) compared to others; wide 'pits' are also evident (red arrows). The EBSD map also shows remnant Zn metal in the regions immediately beneath the original Zn wire surface.

sectioning with EBSD. Corrosion features on the basal plane {0001} (hkl {001}), the prismatic plane I {10-10} (hkl {100}), the prismatic plane II {11-20} ({hkl 110}), the pyramidal plane I {10-11} (hkl 101) and the pyramidal plane II {11-22} (hkl{112}) were characterised, as shown in Figure 6 and Figure 7.

From this work it can be observed that the striation-like corrosion features (yellow arrows in Figure 6) are more
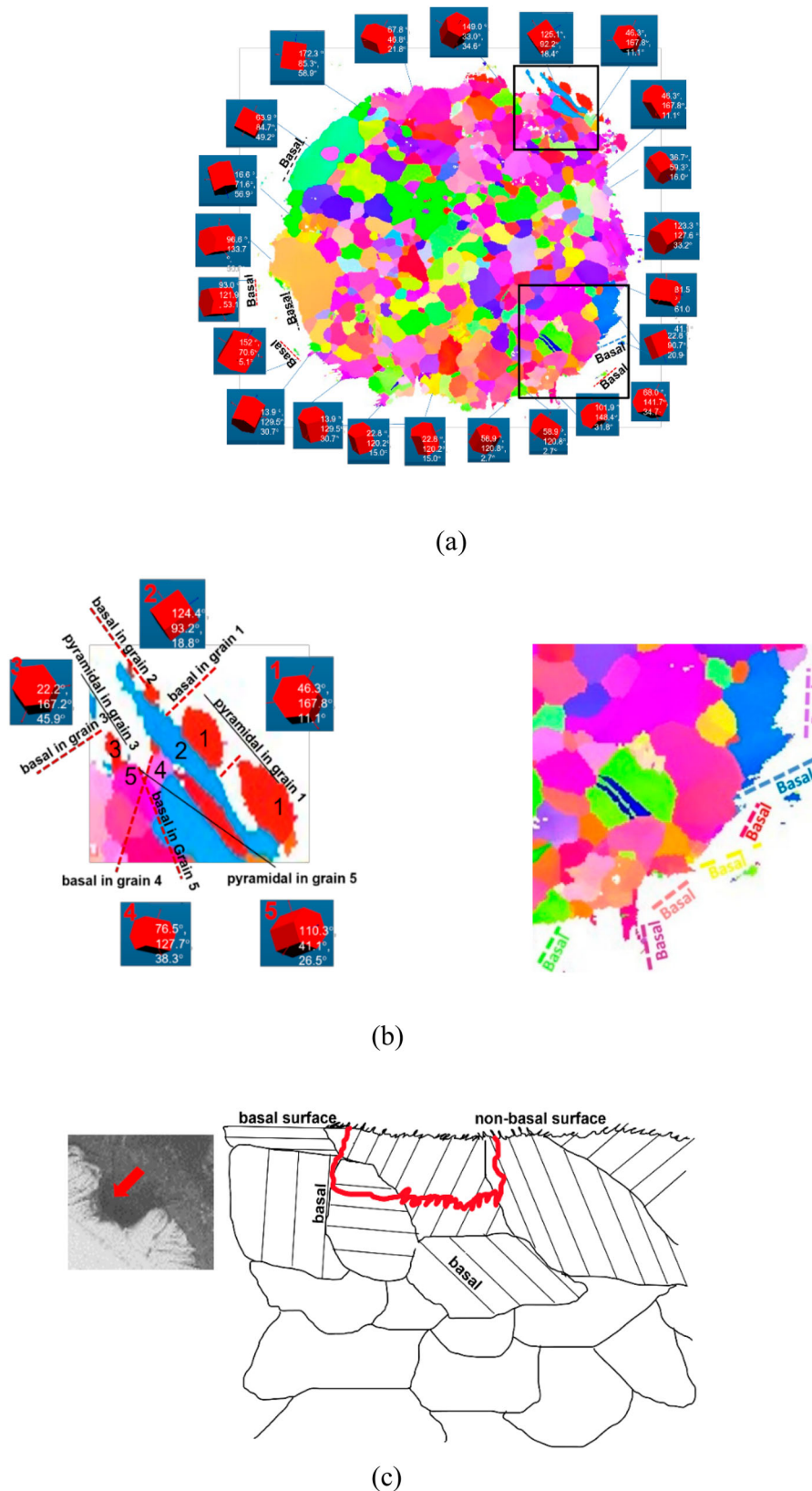
(a)

(b)

(c)

Figure 7. Analysis of crystallographic orientation of the corrosion attack where red dashed lines indicate the trace of basal planes and black lines the prismatic planes. (a) EBSD orientation analysis for all the exposed grains showing the relation between corrosion and orientation, (b) Trace analysis reveals that corrosion develops preferentially on non-basal planes leaving 'edges/blades' lying perpendicular to [0001], (c) schematic representation showing preferential surface attack, as well as the formation of deep pits (red lines) similar to that shown inset (region from Figure 4a).

pronounced for some grains than others. In fact some grains appear more resistant and others appear less resistant. Wide 'pits' (Red arrow in Figure 6) were also observed on some grains along the circumference of the wire corrosion front.

The nature of crystallographic attack is revealed by cross-sectional EBSD. The cross-sectional image in

Figure 7a shows a typical example of an EBSD map extracted from the serial cross-sectional EBSD analysis carried out for successive sections along the length of the wire. The corrosion features, namely the wide 'pits' and striations, were matched with specific planes, i.e. the basal planes, prismatic planes and pyramidal
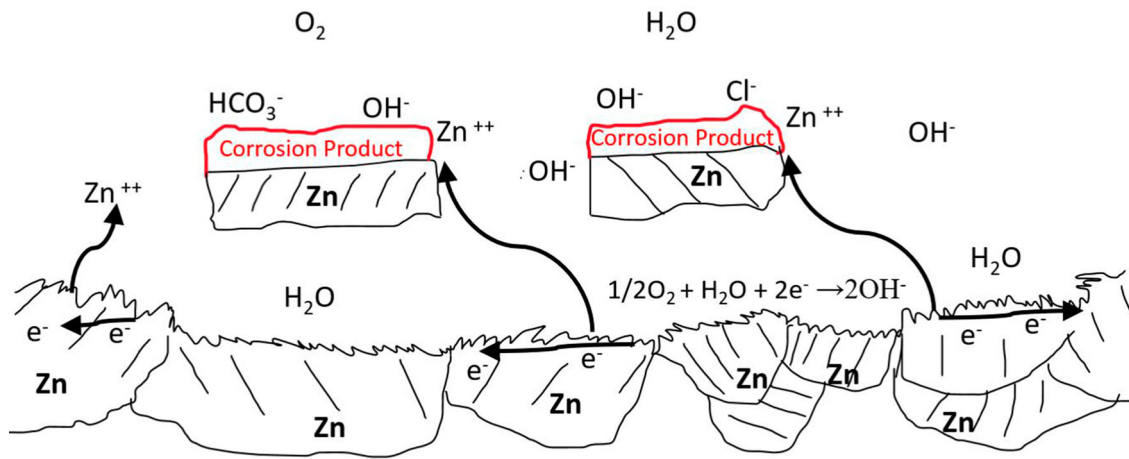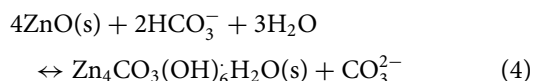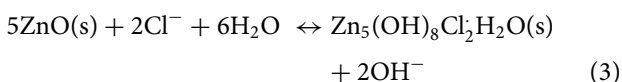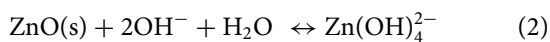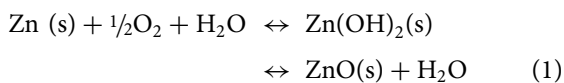
Figure 8. Schematic representation of the corrosion process resulting in remnant Zn.

planes where the red dashed lines show the orientation of the basal planes. Figure 7a shows that grain surfaces oriented with the basal planes facing the corrosion media tend to appear relatively flat compared to other grain orientations. Corrosion striations are most commonly observed on grains having a non-basal plane facing the corrosion media. Figure 7b shows a higher magnification trace analysis confirming that the basal planes are the least attacked and the striation-like topographical appearance is the result of preferential attack on higher index planes.

Discussion

The remnant Zn embedded in the corrosion products in the region immediately beneath the initial zinc wire surface (Figure 2) probably arises due to the cumulative effect of the differential corrosion attack and corrosion product formation from the initial corrosion process onwards. The Zn surface may initially react with the environment to create zinc oxide, zinc hydroxide, simonkolleite or zinc hydroxy carbonate [2]:

$$Zn\ (s) + \tfrac{1}{2}O_2 + H_2O \ \leftrightarrow\ Zn(OH)_2(s)$$
$$\leftrightarrow\ ZnO(s) + H_2O \qquad (1)$$

$$ZnO(s) + 2OH^- + H_2O \ \leftrightarrow\ Zn(OH)_4^{2-} \qquad (2)$$

$$5ZnO(s) + 2Cl^- + 6H_2O \ \leftrightarrow\ Zn_5(OH)_8Cl_2.H_2O(s)$$
$$+ 2OH^- \qquad (3)$$

$$4ZnO(s) + 2HCO_3^- + 3H_2O$$
$$\leftrightarrow\ Zn_4CO_3(OH)_6H_2O(s) + CO_3^{2-} \qquad (4)$$

The corrosion product $Zn(OH)_2$, $Zn_5(OH)_8Cl_2.H_2O$, and $Zn_4CO_3(OH)_6H_2O$ formed on the surface may be beneficial to the corrosion resistance of the zinc[29,30], as indicated in Figure 2. Higher O and C concentrations were detected at the outer most surface of the zinc wire (Figure 2a,b). This indicates a dense thin layer of oxide/hydroxide or carbonate formed at the surface during the initial corrosion process. The dense hydroxide/oxide and carbonate may protect the zinc so that it is not attacked as quickly as other areas where the dense layer has not formed or has been broken (Figure 2c). As the corrosion progress, the corrosive media

can penetrate the protective corrosion product where its thickness is less or where it can penetrate through cracks in the initial protective dense thin layer, hence dissolving the zinc metal beneath the cracked thin protective layer. Figure 2a shows that the remnant Zn lying at the initial Zn wire surface typically has its basal plane facing the corrosive media. We anticipate it is the combined result of (1) the intact initial protection layer formed on the surface, (2) the difficulty of dissolution on the surface grains with basal planes facing outwards [7], and (3) micro-galvanic cells formed between the remanent grains and surrounding grains galvanically protecting the remnant grains [31]. As the corrosion propagates the surrounding grains are consumed but leaving the grains having basal planes facing the corrosion media (Figure 8). Nevertheless, the hypothesis of the micro-galvanic protection needs more in-depth investigation.

Here we find that crystallographic corrosion occurs on zinc under the initial oxide/hydroxide film [32,2]. Further, the crystallographic analysis has indicated preferential attack on pyramidal and prismatic planes, which is consistent with the studies by Abayarathna et al. [5] on zinc without surface film in different testing media, where they found the corrosion attack was predominantly on {11-20}surfaces.

It is known that crystallographic orientation is important in corrosion dissolution or oxidation [33,34]. The influence of crystallographic orientation is believed to be related to the binding energy of the surface atoms [34,30]. The close-packed basal planes have a higher atomic coordination number with higher binding energy and are thought to have superior corrosion resistance, thus less 'penetration' into the grain, as observed in Figure 7b. Taking the zinc cell parameters $a = 0.266$nm, $c = 0.495$nm, $\alpha = 90°$, $\gamma = 120°$, the atomic surface density is highest on the basal plane (0001) of $1.89e^{-5}$ atoms/nm^2, followed by the prismatic plane I (01-10) and the pyramidal plane I of $0.75e^{-5}$ atoms/nm^2, the prismatic plane II(11-20) of $0.43e^{-5}$ atoms/nm^2, and the pyramidal plane II of $0.38e^{-5}$ atoms/nm^2. Since the basal plane has nearly three to five times higher atomic packing density than the other planes, thus lower surface energy or higher activation energy for disolution is expected on basal planes. As a result, the basal planes dissolve slower than the other planes. This results in easier development of corrosion attack on non-basal planes which propagates into the grain leaving basal planes less attacked.

Thus, the wide 'pits' (Figure 4) might be formed as the result of increased corrosion rate on non-basal planes for favourably oriented grains. This is clearly shown in Figure 7b where a wide pit is formed between grains 2 and 5 due to faster dissolution of grains 3 and 4.

As summarised in the Results section, in addition to the wide 'pits', very narrow and deep 'pits', i.e. striations, were observed on non-basal planes. The striations have formed as a result of preferential dissolution of non-basal planes. Figure 7c illustrates the corrosion developed on surfaces with basal and non-basal planes where striations are developed on non-basal planes whilst the basal plane is relatively flat. On non-basal planes, the lateral propagation of corrosion encounters more resistance for (0001). Consequently, the less attacked zinc volumes are left behind as plates and the more attacked volumes appear as grooves, resulting in striations on the corroding surface. As a result the surface striations lie on the trace of the (0001) with the surface. This observation agrees with Abayarathna et al. [5] who also found the corrosion attack is least on {0001}. As for a randomly textured crystalline aggregate the probability of basal planes facing the corrosion media is less than that of non-basal planes in HCP metals, most of the corroded surface of the Zn wire exhibit striations (Figure 5b). The striations reflect the underlying grain orientation.

Conclusions

In this study a zinc wire has been allowed to corrode extensively (under a moderate anodic potential) in order to study the nature of corrosion attack that occurs under the original oxide/hydroxide film. The key findings of this study are:

1) Due to considerably faster milling rate of pFIB, large area (500μm diameter) EBSD crystallographic analysis has been achieved, providing a detailed overview of the nature of the crystallographic corrosion process.
2) In common with recent literature the corrosion products consist of three layers, namely (from the outside), a porous layer, a dense layer within the original boundary of the metal surface, and the attacked layer. There are substantial differences in the porosity and density between the layers, with the porous layer having the highest porosity and the dense layer the lowest porosity.
3) Corrosion occurs under the initial surface film. The corrosion rate of the basal planes is lower than that of the non-basal planes, which can result in wide 'pits' due to the accelerated corrosion of some grains.
4) The uncorroded plates are the result of preferential dissolution of non-basal planes and so are parallel to the basal plane. As a result, the surface striations reflect the trace of the intersection of the (0001) planes with the surface.
5) A discontinous ring of remnant metallic Zn was detected immediately beneath the original zinc wire boundary. This could be due to a combined effect of the initial protective film on the surface and the crystallographic corrosion.

Acknowledgements

Disclosure statement

Funding

ORCID

Xiangli Zhong http://orcid.org/0000-0003-4772-1158

References

[1] Bernard MC, Goff AH, Phillips N. In situ Raman study of the corrosion of zinc coated steel in the presence of chloride: II. Mechanisms of underpaint corrosion and role of the conversion layers. J Electrochem Soc 1995;142(7):2167–2170. doi:10.1149/1.2044269

[2] Ramanauskas R, Juškenas R, Kaliničenko A, et al. Microstructure and corrosion resistance of electrodeposited zinc alloy coatings. J Solid State Electrochem 2004;8(6):416–421. doi:10.1007/s10008-003-0444-2

[3] Crundwell FK. Kinetics and mechanism of the oxidative dissolution of a zinc sulphide concentrate in ferric sulphate solutions. Hydrometallurgy. 1987;19(2):227–242. doi:10.1016/0304-386X(87)90007-7

[4] Graedel TE. Corrosion mechanisms for zinc exposed to the atmosphere. J Electrochem Soc 1989;136(4):193C–203C. doi:10.1149/1.2096868

[5] Abayarathna D, Hale EB, O'Keefe TJ, et al. Effects of sample orientation on the corrosion of zinc in ammonium sulfate and sodium hydroxide solutions. Corros Sci 1991;32(7):755–768. doi:10.1016/0010-938X(91)90089-8

[6] Park CJ, Lohrengel MM, Hamelmann T, et al. Grain-dependent passivation of surfaces of polycrystalline zinc. Electrochim Acta. 2002;47(21):3395–3399. doi:10.1016/S0013-4686(02)00221-9

[7] Khorsand S, Raeissi K, Golozar MA. An investigation on the role of texture and surface morphology in the corrosion resistance of zinc electrodeposits. Corros Sci 2011;53(8):2676–2678. doi:10.1016/j.corsci.2011.04.007

[8] Chandrasekar MS, Pushpavanam M. Synergetic effects of pulse constraints and additives in electrodeposition of nanocrystalline zinc: Corrosion, structural and textural characterization. Mater Chem Phys 2010;124(1):516–528. doi:10.1016/j.matchemphys.2010.07.004

[9] Shkirskiy V, Yule LC, Daviddi E, et al. Nanoscale scanning electrochemical cell microscopy and correlative surface structural analysis to Map anodic and cathodic reactions on polycrystalline Zn in acid media. J Electrochem Soc 2020;167(4):0041507. doi:10.1149/1945-7111/ab739d

[10] BlueScope Steel. "Corrosion. Corrosion Resistance of Zinc in Water," Tech. Bull. CTB-05, pp. 1–2.

[11] Mena E, Veleva L, Souto RM. Mapping of local corrosion behavior of zinc in substitute ocean water at its initial stages by SVET. Int J Electrochem Sci. 2016;11:5256–5266. doi:10.20964/2016.06.50

[12] Cole IS, Ganther WD, Furman SA, et al. Pitting of zinc: Observations on atmospheric corrosion in tropical countries. Corros Sci 2010;52(3):848–858. doi:10.1016/j.corsci.2009.11.002

[13] Cole IS, Electrochem J, Soc C. Products formed during the interaction of seawater droplets with Zinc surfaces: II. Results from short exposures products formed during the interaction of seawater droplets II. J Electrochem Soc 2010;157:C213. doi:10.1149/1.3391383

[14] Wang YD, Yang YS, Cole I, et al. Investigation of the microstructure of an aqueously corroded zinc wire by data-constrained modelling with multi-energy X-ray CT. Mater Corros 2013;64(3):180–184. doi:10.1002/maco.201106341

[15] Silva Filho JF, Lins VFC. Crystallographic texture and morphology of an electrodeposited zinc layer. Surf. Coatings Technol. 2006;200 (9):2892–2899. doi:10.1016/j.surfcoat.2005.04.032

[16] Nowell MM, Witt RA, True BW. Ebsd sample preparation: techniques, tips, and tricks. Micros. Today. 2005;13(4):44–49. doi:10.1017/S1551929500053669

[17] Guo J, Amira S, Gougeon P, et al. Effect of the surface preparation techniques on the EBSD analysis of a friction stir welded AA1100-B4C metal matrix composite. Mater Charact 2011;62(9):865–877. doi:10.1016/j.matchar.2011.06.007

[18] Chen YJ, Hjelen J, Roven HJ. Application of EBSD technique to ultrafine grained and nanostructured materials processed by severe plastic deformation: Sample preparation, parameters optimization and analysis. Trans. Nonferrous Met. Soc. China 2012;22(8):1801–1809. doi:10.1016/S1003-6326(11)61390-3

[19] Zhong X, Burke MG, Withers PJ, et al. Multi-modal plasma focused ion beam serial section tomography of an organic paint coating. Ultramicroscopy. 2017;197:1–10. doi:10.1016/j.ultramic.2018.10.003

[20] Schindelin J, Arganda-Carreras I, Frise E, et al. Fiji: An open-source platform for biological-image analysis. Nat Methods. 2012;9(7):676–682. doi:10.1038/nmeth.2019

[21] WM Haynes E. Crc handbook of chemistry and physics. CRC Press; Boca Raton, Florida, 2011.

[22] Burnett TL, Winiarski B, Kelley R, et al. Xe+ plasma FIB: 3D microstructures from nanometers to hundreds of micrometers. Micros Today. 2016;24(03):32–39. doi:10.1017/S1551929516000316

[23] Rubanov S, Munroe PR. FIB-induced damage in silicon. J Microsc 2004;214(3):213–221. doi:10.1111/j.0022-2720.2004.01327.x

[24] Michael JR, Giannuzzi LA, Burke MG, et al. Mechanism of FIB-induced phase transformation in austenitic steel. Microsc Microanal 2022;28(1):70–82. doi:10.1017/S1431927621013738

[25] Zhong X, Wade CA, Withers PJ, et al. Comparing Xe+pFIB and Ga+FIB for TEM sample preparation of Al alloys: Minimising FIB-induced artefacts. J Microsc 2021;282(2):101–112. doi:10.1111/jmi.12983

[26] Ziegler JF, Ziegler MD, Biersack JP. Nuclear Instruments and Methods in physics research B SRIM – The stopping and range of ions in matter (2010). Nucl. Inst. Methods Phys. Res. B. 2010;268(11–12):1818–1823. doi:10.1016/j.nimb.2010.02.091

[27] "Scanning - 2007 - Drouin - CASINO V2 42 A Fast and Easy-to-use Modeling Tool for Scanning Electron Microscopy and.pdf.".

[28] Zhong XL, Haigh SJ, Zhou X, et al. An in-situ method for protecting internal cracks/pores from ion beam damage and reducing curtaining for TEM sample preparation using FIB. Ultramicroscopy. 2020;219(October):113135. doi:10.1016/j.ultramic.2020.113135

[29] Han G, Lee J-Y, Kim Y-C, et al. Preferred crystallographic pitting corrosion of pure magnesium in Hanks' solution. Corros Sci 2012;63:316–322. doi:10.1016/j.corsci.2012.06.011

[30] Pawar S, Slater TJA, Burnett TL, et al. Crystallographic effects on the corrosion of twin roll cast AZ31 Mg alloy sheet. Acta Mater 2017;133:90–99. doi:10.1016/j.actamat.2017.05.027

[31] Song GL, Mishra R, Xu Z. Crystallographic orientation and electrochemical activity of AZ31 Mg alloy. Electrochem Commun 2010;12(8):1009–1012. doi:10.1016/j.elecom.2010.05.011

[32] Ramanauskas R. Structural factor in Zn alloy electrodeposit corrosion. Appl Surf Sci 1999;153(1):53–64. doi:10.1016/S0169-4332(99)00334-7

[33] Ramanauskas R, Quintana P, Maldonado L, et al. Corrosion resistance and microstructure of electrodeposited Zn and Zn alloy coatings. Surf. Coatings Technol. 1997;92(1–2):16–21. doi:10.1016/S0257-8972(96)03125-8

[34] Liu M, Qiu D, Zhao M, et al. The effect of crystallographic orientation on the active corrosion of pure magnesium. Scr Mater. 2008;58:421–424. doi:10.1016/j.scriptamat.2007.10.027